Wave runup on composite beaches and dynamic cobble berm revetments

Blenkinsopp, C.E.[a], Bayle, P.M.[a,b,c], Martins, K.[a,d], Foss, O.W.[a], Almeida, L-P[e,f], Kaminsky, G.M.[g], Schimmels, S.[h] & Matsumoto, H[i].

a. Centre for Infrastructure, Geotechnics and Water Engineering, Department of Architecture and Civil Engineering, University of Bath, Bath BA2 7AY, UK. c.blenkinsopp@bath.ac.uk; p.m.bayle@bath.ac.uk; o.foss@bath.ac.uk
b. BRGM, Regional Direction Nouvelle-Aquitaine, Pessac, France. p.bayle@brgm.fr
c. IFREMER Arcachon, 33120 Arcachon, France.
d. UMR 5805 EPOC, CNRS - University of Bordeaux, Allée Geoffroy Saint-Hilaire, F-33615 Pessac, France. kevin.martins@u-bordeaux.fr
e. Universidade Federal do Rio Grande (FURG), Campus Carreiros, Instituto de Oceanografia, Avenida Italia, Km 8 96203-900, Rio Grande, RS, Brasil. melolp@gmail.com
f. +ATLANTIC LVT, Edifício LACS Estrada da Malveira da Serra 920 2750-834 Cascais, Portugal.
g. Washington State Department of Ecology, Olympia, WA, USA. george.kaminsky@ecy.wa.gov
h. Forschungszentrum Küste (FZK), Leibniz University Hannover & Technische Universität Braunschweig, Merkurstraße 11, 30419 Hannover, Germany. schimmels@fzk.uni-hannover.de
i. Scripps Institution of Oceanography, University of California, San Diego, La Jolla, CA, USA. himatsumoto@ucsd.edu

Abstract

The effects of climate change and sea level rise, combined with overpopulation are leading to ever-increasing stress on coastal regions throughout the world. As a result, there is increased interest in sustainable and adaptable methods of coastal protection. Dynamic cobble berm revetments consist of a gravel berm installed close to the high tide shoreline on a sand beach and are designed to mimic naturally occurring composite beaches (dissipative sandy beaches with a gravel berm around the high tide shoreline). Existing approaches to predict wave runup on sand or pure gravel beaches have very poor skill for composite beaches and this restricts the ability of coastal engineers to assess flood risks at existing sites or design new protection structures. This paper presents high-resolution measurements of wave runup from five field and large-scale laboratory experiments investigating composite beaches and dynamic cobble berm revetments. These data demonstrated that as the swash zone transitions from the fronting sand beach to the gravel berm, the short-wave component of significant swash height rapidly increases and can dominate over the infragravity component. When the berm toe is submerged at high tide, it was found that wave runup is strongly controlled by the water depth at the toe of the gravel berm. This is due to the decoupling of the significant wave height at the berm toe from the offshore wave conditions due to the dissipative nature of the fronting sand beach. This insight, combined with new methods to predict wave setup and infragravity wave dissipation on composite beaches is used to develop the first composite beach/dynamic revetment-specific methodologies for predicting wave runup.

Keywords

Wave runup; Swash; Dynamic cobble berm revetment; Dynamic revetment; Composite beach; Wave reflection

1. Introduction

Significant progress towards a better understanding of morpho- and hydrodynamic processes on sandy, and to a lesser extent gravel beaches has been made over the past few decades through a variety of laboratory, field and numerical investigations. Knowledge of mixed beaches which contain both sand and gravel is less well advanced however, due largely to the greatly increased complexity introduced by bi- or multimodal sediment size distributions. Despite the presence of sand, mixed beaches are commonly considered to be a type of gravel beach, which were divided into three sub-categories by Jennings and Schulmeister (2002): (1) pure gravel beaches which are not strictly "mixed" and are dominated by gravel throughout their profile, (2) mixed sand and gravel beaches which are composed of fully mixed gravel and sand, and (3) composite gravel beaches which have a two-part profile consisting of a steep upper foreshore or backshore gravel ridge fronted by a lower-gradient sand slope. Note that following the Wentworth (1922) grain size classification, the term gravel is used to describe coarse sediments in the size range 2 mm < D_{50} < 256 mm which is subdivided into granules (2 mm < D_{50} < 4 mm), pebbles (4 mm < D_{50} < 64 mm) and cobbles (64 mm < D_{50} < 256 mm).

This study focusses specifically on a subset of composite beaches (type 3; Jennings and Schulmeister, 2002) that exhibit a permanent ridge of pebbles and/or cobbles situated around mean high water (MHW) with a clear delineation between the sand and gravel. Such beaches were first defined in the literature by Carter and Orford (1993) and are commonly found in the UK, USA (West Coast), New Zealand and Ireland. Note that composite beaches with seasonally transient backshore cobble berms and with isolated patches of cobbles over the foreshore (e.g. Matsumoto et al., 2020) have also been identified in the literature. Also, gravel beaches that are sandy below mean low water (MLW) are common on the south coast of England (e.g. Karunarathna et al., 2012; Watt et al., 2008). While such beaches are expected to have similarities with composite beaches as defined here, they are not directly considered in this work.

Komar (2005) highlights that composite beaches differ from mixed sand and gravel beaches (e.g. type 2; Jennings and Schulmeister, 2002) primarily due to the bimodal nature of the sediment size distribution and a much higher proportion of sand relative to coarse material. Cross-shore sorting by waves leads to a highly dissipative lower foreshore of sand ($\tan\beta_{sand}$ ≈ 0.01 to 0.05) that is exposed except at high tide, backed by a steep, permeable and reflective backshore ridge of cobbles ($\tan\beta_{berm}$ ≈ 0.1 to 0.25). The differences in the slope, roughness, permeability, and groundwater characteristics of the sand and gravel components of composite beaches means that both the hydro and morphodynamics vary with water level and they behave differently to both pure sand and pure gravel beaches. Effectively, composite beaches represent a combination of the two most stable states at either end of the morphodynamic classification of Wright and Short (1984), making them relatively stable in response to changing hydrodynamic conditions. The dissipative sand beach component exhibits lower mobility because the low gradient promotes a wide surf zone, within which wave energy is gradually dissipated leading to smaller short-wave heights at the shoreline. The steep cobble ridge derives its stability primarily from its porous nature which promotes swash asymmetry (Masselink and Li, 2001). By contrast, mixed sand and gravel beach morphologies tend to be more variable as the more uniform grain size distribution means smaller grains fill the voids between the larger clasts, reducing the porosity of the beach and hence swash asymmetry.

Improved knowledge of composite beach processes is valuable because such beaches are relatively common and are known to be resilient to extreme waves and water levels, but are under-researched. Furthermore, the inherent stability of composite beaches under large storm waves and

the overtopping protection provided by the gravel ridge to the hinterland has inspired coastal engineers to nourish beaches using gravel or cobbles. The structure created is commonly called a dynamic revetment, although this term has been used to describe a wide range of structures from gravel beaches (e.g. Tomasicchio et al., 2010) to cobble berms (e.g. Everts et al., 2002). A summary of these structures is provided by Bayle et al. (2020), however in line with the definition of composite beaches considered here, this paper will consider the sub-category termed dynamic cobble berm revetments by Bayle et al. (2020). These structures are effectively cobble berms constructed around or above the shoreline at mean high water (MHW) to create an artificial composite beach. A small number of such structures currently exist, primarily on the west coast of the USA (e.g. Komar and Allan, 2010; Allan et al., 2005, 2012; Allan and Gabel, 2016; Kaminsky et al., 2020; Everts et al., 2002), however guidance to design them is limited and relatively little monitoring of their performance has been undertaken. Some more recent studies have undertaken large scale laboratory (Bayle et al., 2020) and field experiments (Allan et al., 2006; Bayle et al., 2021) designed to investigate revetment morphodynamics, wave overtopping, wave-by-wave sediment fluxes and cobble transport using tracked cobbles.

For resilient design of dynamic cobble berm revetments, robust predictions of wave runup are essential, but as detailed in Section 2 below, are not currently available. This paper will investigate the different processes which contribute to wave runup including short wave and infragravity swash as well as wave setup using multiple field and large-scale laboratory datasets. The insight gained from this analysis is then used to develop new approaches for estimating wave runup on composite beaches and dynamic cobble berm revetments. The manuscript is organised as follows. Section 2 summarises existing studies of wave runup that are relevant to composite beaches. Section 3 introduces the different field and laboratory experiments from which the data analysed in this paper were obtained and outlines the analysis methods. Section 4 presents new measurements of swash motions and infragravity waves at the shoreline on composite beaches. The discussion in Section 5 develops three new approaches of varying complexity to estimate wave runup on composite beaches based on the results presented in Section 4 and conclusions are provided in Section 6.

2. Wave Runup on Composite Beaches

Swash processes are the primary driver of morphology change on composite beaches and large wave runup events can overtop or overwash the gravel ridge at high tide, which in extreme cases can lead to barrier breaching. While many empirical equations to predict wave runup on sandy beaches are available, no composite beach-specific studies of runup have been undertaken.

A variety of investigators have examined wave runup on gravel and mixed beaches. Kirk (1975) presented measurements of wave runup on a mixed sand and gravel beach and found breaker height to be the primary controlling factor. Powell (1990) developed a predictor for runup on gravel beaches based on laboratory and field data. Bayle et al. (2020) measured wave runup on a dynamic cobble berm revetment in a large-scale laboratory experiment and demonstrated that extreme runup represented by $R_{2\%}$ - the elevation exceeded by 2% of wave runup events - was reduced compared to an equivalent sand beach. Billson et al. (2019) measured the infragravity component of swash on 5 beaches, including two wind-wave dominated composite beaches. They found that shoreline infragravity energy was low at these sites and existing predictive equations based on offshore wave conditions had mixed skill with reasonable performance at one beach (Minsmere) and no skill at the other (Camber). Poate et al. (2016) used extensive field measurements from gravel beaches in the UK along with synthetic runup data generated using the XBeach-G numerical model to develop new runup predictors for pure gravel beaches with the form:

$$R_{2\%} = C_p H_0 \tan\beta_{gravel}^{0.5} T \quad (1)$$

where $\tan\beta_{gravel}$ is the gravel beach slope, H_0 is the deepwater significant wave height and T is either the mean zero-crossing (T_z) or peak (T_p) wave period for which different values of the constant C_p were presented (C_p = 0.49 or 0.33 respectively). It is noted that the field data from two composite beach sites: Westward Ho! and Seascale were eliminated from the analysis because the recorded runup values were notably smaller than those recorded on the pure gravel beaches due to the dissipative nature of the sandy lower profile, thus Eq. 1 is not considered appropriate for composite beaches.

If we consider composite beach ridges or dynamic revetments as coastal structures, a range of wave runup equations for sloping coastal defence structures exist and typically estimate wave runup based on the wave height at the structure toe (e.g. EurOtop, 2018). The EurOtop manual provides a general equation to predict wave runup on coastal structures:

$$\frac{R_{2\%}}{H_{m0}} = 1.65\gamma_f \xi_{m-1,0} \quad (2)$$

where H_{m0} is the spectral significant wave height at the toe of the structure, γ_f is a reduction factor to account for the slope roughness and $\xi_{m-1,0}$ is the Irribarren number based on the mean spectral wave period $T_{m-1,0}$ to calculate wavelength ($\xi_{m-1,0} = \frac{tan\beta_{struct}}{2\pi H_{m0}/(gT_{m-1,0}^2)}$). Little work has been done to determine suitable values of γ_f for gravel or cobble slopes, although recent numerical work by Zaalberg (2019) suggested values between 0.62 and 0.75 for a dynamic cobble berm revetment.

An earlier version of the EurOtop manual (EurOtop, 2007) also includes an expression for wave runup on gravel beaches where it is assumed that the crest elevation of a gravel beach h_c is approximately equal to the elevation of the largest wave runup events and could approximate $R_{2\%}$:

$$R_{2\%} \approx h_c = C_e H_{m0} \sqrt{s_{om}} \quad (3)$$

where H_{m0} is the spectral significant wave height at the toe of the gravel, s_{om} is the wave steepness calculated using the mean wave period T_z and C_e is a constant which was given the value C_e = 0.3. Polidoro et al. (2014) applied Eq. 3 at a gravel beach at Worthing, UK and found it to overpredict wave runup, however they used spectral significant wave height in deep water, potentially leading to the overprediction.

No method to predict wave runup on composite beach ridges and dynamic revetments currently exists. The summary above details existing approaches to predict wave runup on beaches and structures with similarities to composite beaches and dynamic revetments. These methods indicate a likely dependence of wave runup on wave height at the cobble berm/dynamic revetment toe but any attempts to apply them to composite beaches have proven unsuccessful. The primary goal of this study is to use new understanding of wave runup processes based on field and laboratory measurements to develop empirical equations capable of predicting wave runup on composite beaches. The ability to estimate wave runup is important for the design of dynamic cobble berm revetments as it gives insight into the crest height and revetment volume required to limit overtopping during high water levels.

3. Methodology

This study utilises inner surf and swash data obtained at 2 composite beach field sites in the UK, a dynamic cobble berm revetment in the USA and 2 large-scale laboratory experiments designed to investigate dynamic cobble berm revetments as summarised below. Hereafter, the term “berm”

refers to either the gravel ridge of a composite beach or a dynamic cobble berm revetment. A list of symbols is provided in Table A1.

3.1 Field Sites

Experiments were conducted at 3 field sites: composite beaches at Saltburn-by-the-Sea and Westward Ho! in England and a dynamic cobble berm revetment at North Cove, USA. Figure 1 presents details regarding the beach morphology, instrument locations, wave conditions and water levels and key parameters for each experiment are given in Table 1. At all sites, wave runup was captured using an elevated 2D scanning Lidar located close to the high tide shoreline (see Fig 1a-c). Note that at all sites, the berm toe is submerged at high tide but exposed at lower tidal elevations.

The Saltburn-by-the-Sea experiment is described in detail by Martins et al. (2017a). Saltburn-by-the-Sea (SALT) is a northeast-facing composite beach in NE England on the North Sea coast. The dissipative sandy foreshore is backed by a rounded pebble berm and a vertical seawall. The toe of the berm is located at approximately neap mean high water (MHWN) and during high tides under non-storm conditions the swash zone falls entirely on the berm without reaching the vertical seawall. The analysis in this paper focusses on 8/4 to 11/4/2016 when there was substantial wave runup on the berm. Wave conditions at the toe of the berm were extracted from the Lidar data.

Wave runup measurements during storm wave conditions were completed at Westward Ho! on 2/11 and 3/11/2013 (Almeida et al., 2017). Westward Ho! (WWH) is a west-facing composite beach that lies within Bideford Bay in SW England. The beach has a wide sandy foreshore, backed by a 6.5 m high berm made of rounded pebbles, cobbles and small boulders. The toe of the berm is located at approximately MHWN and during high tides incoming bores collapse directly onto the berm and the swash zone is entirely confined to the berm. In addition to the Lidar, three pressure transducers (PTs) were deployed on the sand beach, including one at the toe of the berm which was used to extract wave data at this location.

An experiment designed to investigate the performance and behaviour of the dynamic cobble berm revetment during storm conditions is described in detail by Bayle et al. (2021). North Cove (NC) is a naturally sandy, west-facing macro-tidal beach in Washington, USA where a dynamic cobble berm revetment has been installed using angular pebbles, cobbles and small boulders to protect the hinterland. The toe of the revetment is located at approximately MHWN and it is backed by a vertical scarp (Fig. 1c). This paper focusses on the period 19/1 to 24/1/2019 when wave runup was recorded on the berm. Wave conditions at the toe of the berm were extracted from the Lidar data.

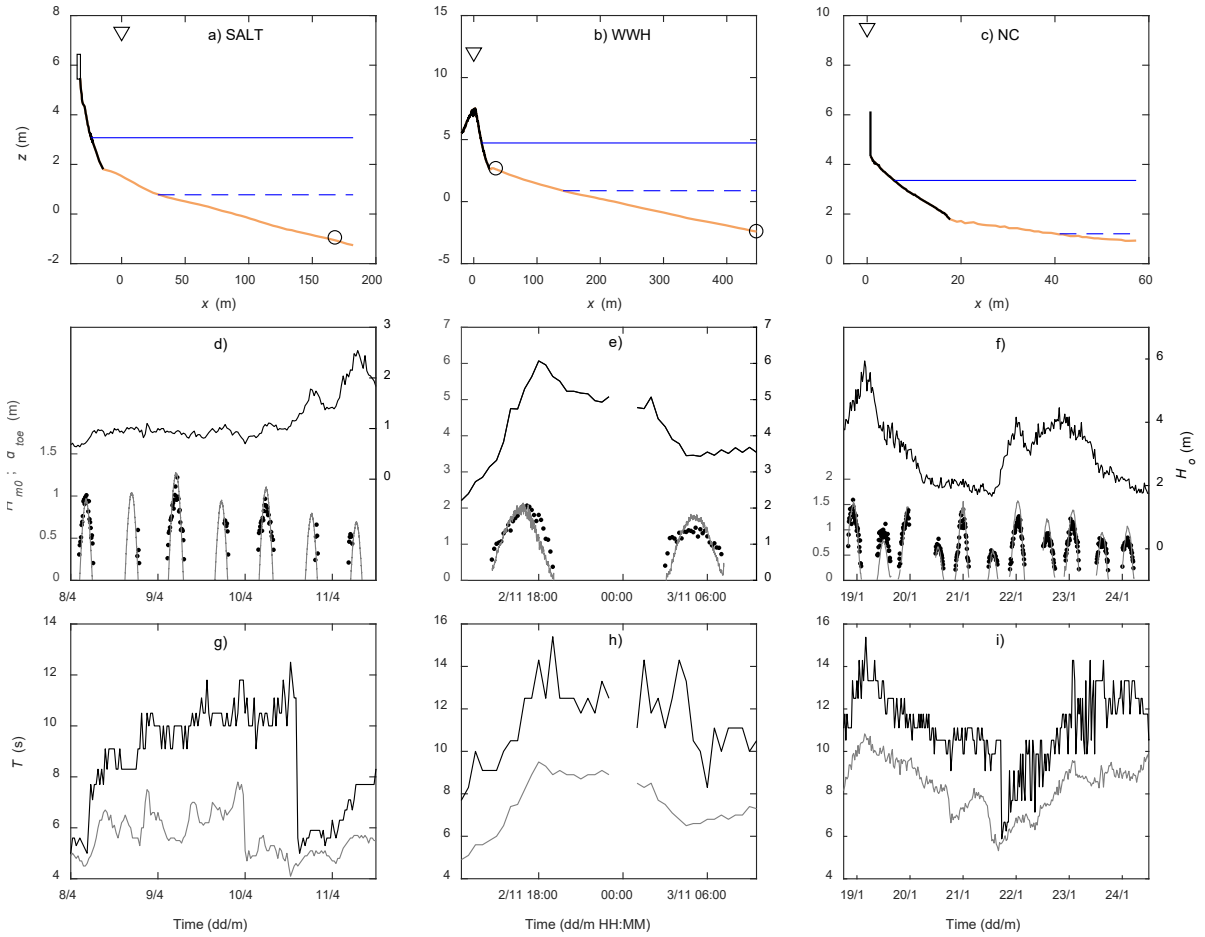

Figure 1: Site geometry (top), wave height and water level data (middle) and wave period data (bottom) for each experiment: Left column shows Saltburn-by-the-Sea (SALT); Middle column shows Westward Ho! (WWH); Right column shows North Cove (NC). **a-c)** Representative beach profiles (orange = sand; black = berm), Lidar positions (▽), PT locations (o), maximum (solid blue line) and mean tidal elevation (dashed blue line) measured during the experiments are shown. Elevations are defined relative to the local survey datums: SALT and WWH = Ordnance Datum (OD) NC = North American Vertical Datum of 1988 (NAVD 88). **d-f)** Primary y-axis: Significant wave height at the berm toe H_{m0} (black dots), water depth at the berm toe d_{toe} (grey solid line). Secondary y-axis: Offshore significant wave height H_o (black solid line). **g-i)** Peak wave period (black line) and mean wave period (grey line).

3.2 Laboratory Experiments

Two experiments (DynaRev1 and 2) designed to investigate the performance of a dynamic cobble berm revetment under a rising water level and varying wave conditions were undertaken in the Large Wave Flume (Großer Wellenkanal, GWK) in Hannover, Germany. Key details of the morphology, sediment and wave parameters during these experiments are summarised in Table 1. In both experiments, wave runup and wave conditions at the revetment toe were measured using a SICK LMS511 2D scanning Lidar located 6.3 m above the revetment toe (z = 11.8 m) at a sample frequency of 25 Hz.

DynaRev1 (DR) is described in detail by Blenkinsopp et al. (2021) and Bayle et al. (2020). A dynamic cobble berm revetment with an initial slope $\tan\beta_{berm}$ = 0.167 and volume of 9.375 m^3 was constructed on a sand beach with gradient $\tan\beta_{sand}$ = 0.067 using rounded, well-sorted cobbles (D_{50} = 63 mm, D_{85}/D_{15} = 1.32) (see Fig. 2a).

DynaRev2 (2DR) used the same experimental methodology and initial revetment design, however the revetment was constructed using angular, poorly-sorted cobbles (D_{50} = 44 mm, D_{85}/D_{15} = 3.79) (see Fig. 2b).

The results presented in this paper for both experiments are confined to a single wave condition (H_s = 0.8 m, T_p = 6.0 s) and water level (z_{WL} = 4.7 m) above the flume bottom. During these tests the wave runup was confined to the seaward-facing slope of the revetment which had steepened from its as-built condition to $\tan\beta_{berm}$ = 0.24 (DR) and 0.3 (2DR).

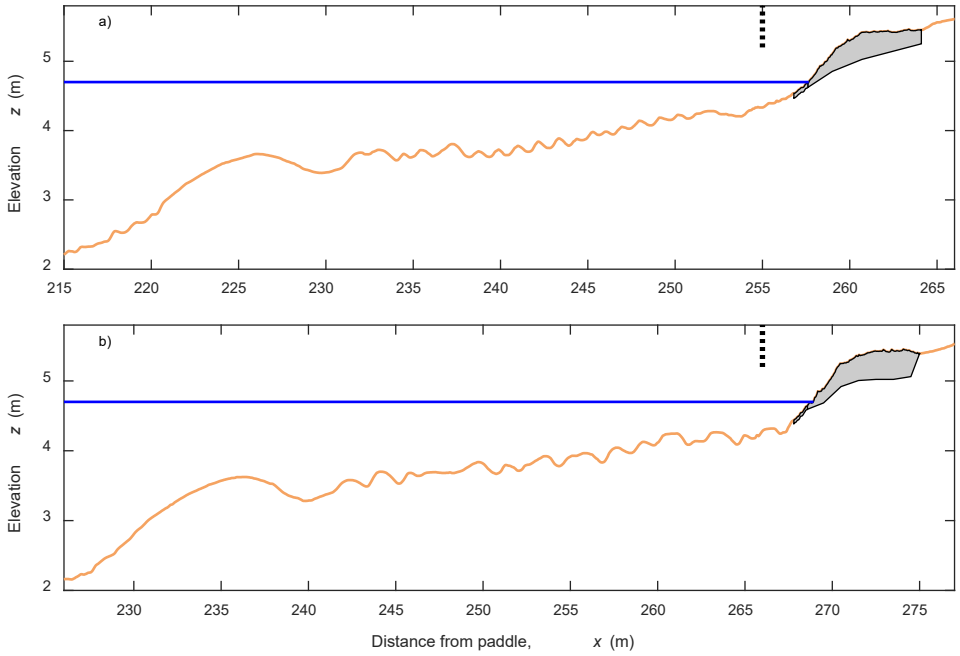

Figure 2: Sandy beach and revetment geometry for **(a)** DynaRev1 and **(b)** DynaRev2 at the start of testing at z_{WL} = 4.7 m. The grey shaded area indicates the revetment volume and the orange line the sand beach profile. The flume bottom provides the vertical datum, z = 0 m. The short vertical dotted lines indicate the centreline of the Lidar field of view.

Table 1: Summary of key morphology, sediment and wave parameters for the field and laboratory (grey shading) experiments.

Experiment	$\tan\beta_{sand}$ ($\tan\beta_{berm}$)	Tidal Range (m)	$D_{50,sand}$ ($D_{50,berm}$) (mm)	H_0 (m)	T_p (s)	H_0/L_0
SALT	0.015 (0.18)	4.6	0.25 (56)	0.65 - 2.54	5 - 12.5	0.004 - 0.033
WWH	0.0125 (0.20)	7.7	0.19 (170)	2.16 - 6.1	7.7 – 15.4	0.002 - 0.042
NC	0.0225 (0.12)	4.3	0.18 (150)	1.8 - 6.0	5.9 – 15.4	0.003 - 0.05
DR	0.067 (0.24)	N/A	0.33 (63)	0.8	6	0.016
2DR	0.067 (0.3)	N/A	0.33 (44)	0.8	6	0.016

3.3 Extraction of wave runup and nearshore wave data

At all sites, wave runup during high-tide periods when swash motions were confined to the berm was measured using elevated 2D Lidar scanners (Fig. 1a-c). As detailed by (Blenkinsopp et al., 2010; Brodie et al., 2015), this approach enables the elevation of the time-varying water surface and intermittently exposed bed to be measured at high spatio-temporal resolution along a cross-shore transect. Each Lidar dataset was converted from polar to cartesian coordinates and interpolated onto a horizontal grid (Δx = 0.1 m). This data was then post-processed using the method of Almeida

et al. (2015) to generate separate timeseries of bed elevation and swash depths. The horizontal shoreline position $X_s(t)$ was taken as the most landward "swash" point at every timestep. The resulting timeseries of horizontal shoreline positions was despiked to remove any spikes larger than 0.5 m that lasted less than 1 s and then filtered using a zero-phase moving average filter. The shoreline positions were then projected onto the berm topography to obtain a timeseries of shoreline elevations $Z_s(t)$, accounting for wave-by-wave changes in bed elevation. Previous authors have used a similar Lidar-based approach to investigate wave runup statistics on gravel beaches (Almeida et al., 2015), sandy beaches (Brodie et al., 2012; Almar et al., 2017), dikes (Hofland et al., 2015) and dynamic cobble berm revetments (Bayle et al., 2020).

For SALT, NC and both DynaRev experiments, spectral significant wave height and time-averaged water depth at the toe of the berm (H_{m0} and d_{toe}) were obtained using Lidar measurements of the time-varying free surface. At WWH the Lidar field of view did not quite extend to the berm toe, as such a pressure transducer with a sampling frequency of 4 Hz was used to measure water depths and wave statistics after applying the non-linear weakly dispersive reconstruction of Bonneton et al. (2018) to account for non-hydrostatic effects (see Fig. 1b for instrument location).

3.4 Wave runup analysis

A schematic detailing key composite beach parameters used in this study is shown in Figure 3. The investigation of wave runup presented below uses an approach similar to that of Stockdon et al. (2006) in their comprehensive analysis of wave runup on sandy beaches. They proposed a general relationship for the elevation of extreme (2% exceedance) runup relative to the still water level (SWL):

$$R_{2\%} = \bar{\eta} + \frac{S}{2} \tag{4}$$

where $\bar{\eta}$ is the wave setup at the shoreline ($\bar{\eta} = \overline{Z_s} - \mathrm{SWL}$) and S represents the significant swash height:

$$S = 4\sqrt{m_0} \tag{5}$$

where m_0 is the zeroth moment of the variance density spectrum $S_{\zeta\zeta}(f)$ computed from the linearly detrended shoreline elevation timeseries $\zeta(t)$. Thus, S is equivalent to four times the standard deviation of $\zeta(t)$.

Stockdon et al. (2006) further decomposed the significant swash height into a short-wave (S_{sw}) and infragravity component (S_{ig}):

$$S = \sqrt{S_{sw}^2 + S_{ig}^2} \tag{6}$$

where S_{sw} and S_{ig} are calculated by applying Eq. 5 only over the appropriate frequencies. For this study a frequency of $0.6f_p$ was used to separate the short-wave and infragravity components of both significant swash (S_{sw} and S_{ig}) and wave height at the berm toe ($H_{m0,sw}$ and $H_{m0,ig}$), where f_p is the discrete peak wave frequency recorded at the offshore waverider buoy at each site. Hamm and Peronnard (1997) and Oh et al. (2020) demonstrated the importance of using a separation frequency which varies with the wave period in the shoaling and surf zones to ensure that short-wave energy is not included in the infragravity band. The separation frequency of $0.6f_p$ used here was chosen based on inspection of the surface elevation spectra at the berm toe at each site.

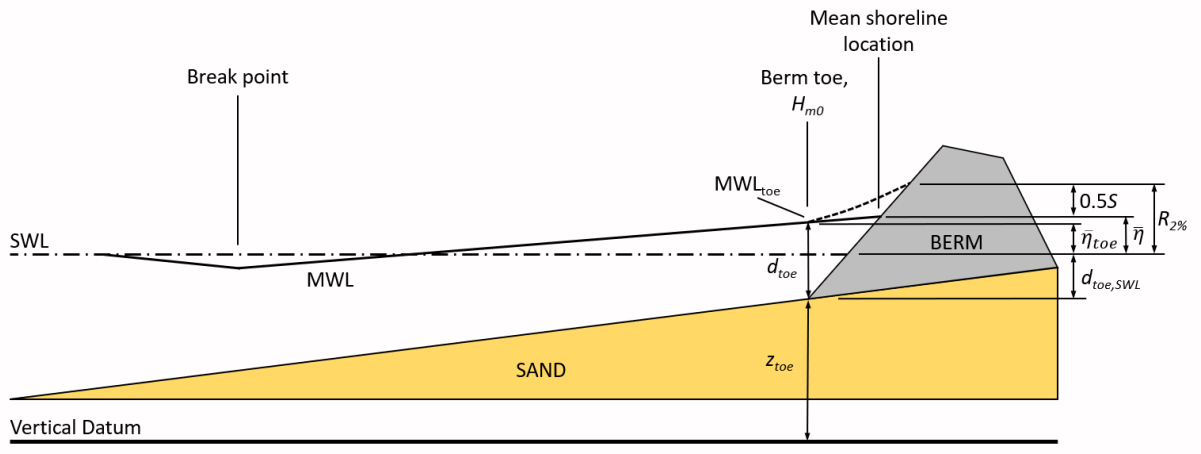

Figure 3: Schematic detailing key composite beach parameters.

Due to the macrotidal nature of the three field sites, wave runup, water depths and wave conditions were evaluated over relatively short 10-minute time windows, to approximate tidal stationarity. This window length was chosen based on a sensitivity analysis and for consistency, 10-minute windows were also used for the DynaRev data. The swash gradient ($\tan\beta_{swash}$) within each time window was taken as the linear gradient within limits defined by ±2σ of the shoreline position timeseries $X_s(t)$ around the mean. The mean water level at the berm toe (MWL_{toe}) is defined here as the 10-minute time-averaged water surface elevation at the location of the toe. The still water level (SWL) is approximated as the time-averaged water surface elevation measured using pressure transducers located seaward of the surf zone at SALT and WWH and wave gauges in the deep-water section of the tank for DR and 2DR (SWL measurements were not possible for NC).

Regression model performance was quantified through the use of the following statistical parameters: root mean square error (RMSE), coefficient of determination (r^2) and normalised mean square error (NMSE) which was calculated as:

$$NMSE = \frac{\frac{1}{N}\sum\left(y_{pred,i}-y_{obs,i}\right)^2}{\sigma^2} \quad (7)$$

where y_{pred} and y_{obs} are the predicted and observed values of a particular parameter, N is the number of observations and σ^2 is the variance of the observed values.

Swash motions on composite beaches and dynamic revetments

The following section investigates the components of the significant swash height (S, S_{sw} and S_{ig}) on composite beaches as a function of the water depth and total, short wave and infragravity spectral significant wave height at the berm toe (H_{m0}, $H_{m0,sw}$, $H_{m0,ig}$). These observations are then used in Section 5.1 to develop new approaches to predict wave runup on composite beaches and dynamic revetments using the framework presented in Section 3.4.

4.1 Variability of swash motions with swash zone position

One of the complexities of runup on a composite beach is that the swash zone transitions from a gently sloping sand beach to the steeper and more porous berm. Previous authors have suggested that the porous nature of pebble/cobble slopes will attenuate wave runup due to high friction and flow volume loss during wave runup (Mason and Coates, 2001). Furthermore, a dependence of runup height on swash slope is a common feature of wave runup equations (e.g. Hunt, 1959; Ruggerio et al., 2001; Stockdon et al., 2006; Poate et al., 2016). This has been primarily linked to the

level of energy dissipation in the surf zone, i.e. dissipation will be larger for milder beach slopes typical of dissipative sand beaches (Brodie et al., 2012; Guedes et al., 2012).

Fig. 4 shows S, S_{sw} and S_{ig} as a function of mean water level relative to the berm toe (MWL_{toe}-z_{toe}, where z_{toe} is the elevation of the berm toe relative to the local datum) at SALT as the swash zone transitioned from the sand beach to the berm during the afternoon rising tide on 9/4/2016. This example is used because SALT is the only field site where swash was measured on both the sand and berm.

MWL_{toe} -z_{toe} is used primarily to indicate the location of the swash zone relative to the berm. When the swash zone is entirely on the sand beach (MWL_{toe} -z_{toe} < -0.45 m), the total significant swash height is dominated by the infragravity component which tends to increase as the water level rises for this tide (Fig. 4). Dominance of infragravity swash on dissipative beaches has been observed by multiple researchers (Guza and Thornton, 1982; Raubenheimer et al., 1996; Ruggiero et al., 2001). The short-wave component of significant swash height S_{sw} is relatively small but increases gradually with MWL_{toe} on the sand beach as the sand gradient, and hence swash slope, increases slightly towards the berm toe. As swashes initially reach the berm toe (-0.45 m < MWL_{toe} -z_{toe} < 0 m) there is no immediate change in the rate of change of S_{sw} with water depth. However, once the mean water depth above the toe surpasses 0 m, the majority of the swash zone is on the berm leading to an increase in swash slope from around 0.02 to 0.06 and S_{sw} becomes strongly controlled by the water depth at the berm toe (see Section 4.2). By contrast, the infragravity significant swash component S_{ig} remains approximately constant as the water depth increases and the swash zone passes onto the berm. As a result, the total significant swash height S becomes dominated by S_{sw}. The trend of increasing S_{sw}/S_{ig} after the swash zone reaches the berm is common to all tides at SALT. The observation that the infragravity component of significant swash height dominates on the sand beach and the short-wave component dominates on the berm is not consistent for all tides, but is the most common behaviour.

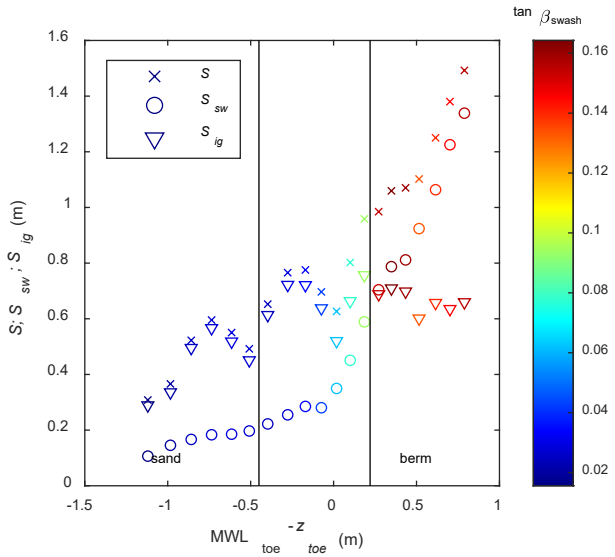

Figure 4: S, S_{sw} and S_{ig} as a function of the elevation difference between the berm toe and MWL_{toe} at SALT as the swash zone transitions from the sand beach to the berm during the afternoon rising tide on 9/4/2016. On the left of the plot, the swash zone is located entirely on sand and on the right, it is entirely on the berm. Between these limits, indicated with the two vertical black lines, swash events pass over both sand and gravel. The colorbar indicates the gradient of the swash zone ($\tan\beta_{swash}$) within each 10-minute time window.

Fig. 5 shows the variation of the significant swash height within the different frequency bands with MWL_{toe} -z_{toe} for all experiments. There is a clear trend that once swash events interact with the berm (MWL_{toe} -z_{toe} > -0.45), S_{sw} increases with mean water level relative to the berm toe for all experiments (Fig. 5b) and this is explained in Section 4.2. Due to the similar berm slopes at SALT ($\tan\beta_{berm}$ = 0.18) and WWH ($\tan\beta_{berm}$ = 0.2) the results fall on approximately the same line, however at the lower gradient NC ($\tan\beta_{berm}$ = 0.133) S_{sw} is smaller for the same value of MWL_{toe} -z_{toe}. Infragravity significant swash heights have a similar magnitude to the short-wave values and a trend of increasing S_{ig} with MWL_{toe} -z_{toe} within each field dataset is evident in Fig. 5c for MWL_{toe} -z_{toe} > -0.45. This may be a function of the reducing surf zone width as the water level rises above the berm toe, leading to lesser dissipation of infragravity energy by short-waves (see Section 4.3). However, it is acknowledged that this observation may be biased by the fact that the WWH data, which includes the largest water depths, was collected during a major storm with offshore significant wave heights up to 6.1 m that would be expected to cause very large infragravity swash (e.g. Guza and Thornton, 1982). The total significant swash height S increases approximately linearly with water depth above the toe for MWL_{toe} -z_{toe} > -0.45 at all field sites.

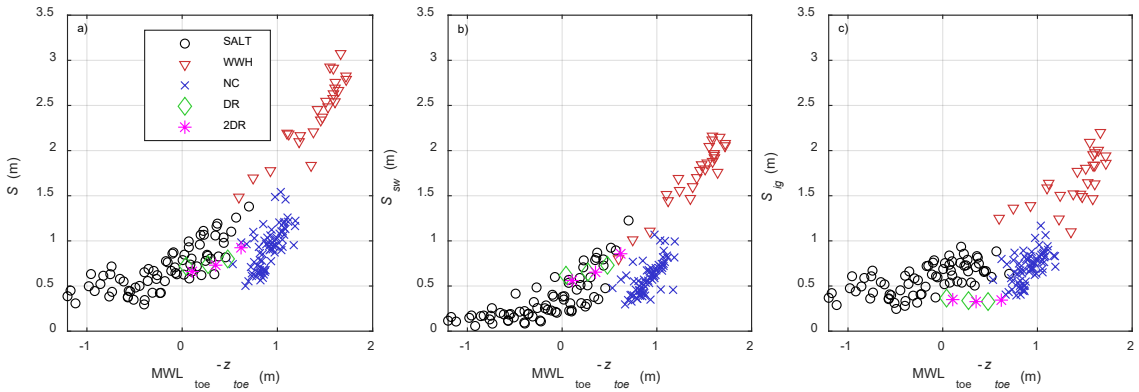

Figure 5: a) Total, **(b)** short-wave, and **(c)** infragravity significant swash height as a function of the elevation difference between the berm toe and MWL_{toe} for all field and laboratory datasets.

4.2 Variability of swash with wave height at the berm toe

The correlation between significant swash height and water depth above the berm toe (Fig. 5) is a result of the fact that the sand slope of composite beaches is typically highly dissipative. The surf zone is saturated at short-wave frequencies which effectively decouples the short-wave height in shallow water from the conditions offshore. Consequently, the height of short-waves, which are a primary driver of swash motions becomes a function of water depth. This is evident in Fig. 1d-f, which shows that the spectral significant wave height measured at the berm toe H_{m0} is approximately equal to the water depth above the berm toe (d_{toe} = MWL_{toe} -z_{toe} for MWL_{toe} -z_{toe} > 0) throughout all three field experiments and is independent of the offshore wave conditions, even when significant wave height in deep water H_o is very large.

To explore this observation, Fig. 6 presents the total, short-wave and infragravity spectral significant wave height at the berm toe (H_{m0}, $H_{m0,sw}$, $H_{m0,ig}$) as a function of water depth at the berm toe d_{toe}. Note that in Fig. 6 and the remainder of this paper, only the 10-minute windows where the swash zone fell entirely on the berm are shown. Thus, there are no values for d_{toe} < 0.26 m.

Fig. 6a and b demonstrate a linear relationship between H_{m0} and $H_{m0,sw}$ with d_{toe}. An apparent relationship between significant infragravity wave height $H_{m0,ig}$ and water depth above the berm toe is also evident in Fig. 6c which is investigated further in Section 4.3. The wave height to water depth

ratio $\gamma_s = H_{m0}/d_{toe}$ is remarkably consistent for all sites ($\gamma_{s,SALT}$ = 0.88; $\gamma_{s,WWH}$ = 0.90; $\gamma_{s,NC}$ = 0.85) with a mean value of γ_s = 0.87 (RMSE = 0.15 m; NMSE = 0.18). These values of γ_s are relatively high compared to previously reported field values and there is no obvious dependence on the gradient of the sand slope seaward of the berm (e.g. Sallenger and Holman, 1985). It is expected that the higher values are caused by proximity of the measurement location to the shoreline and possibly the contribution of reflections from the steep berm. A similar effect was observed by Martins et al. (2017b) for a reflective sand beach in a large-scale laboratory wave flume. Mean values of γ_s for the short-wave and infragravity components of significant wave height are $\gamma_{s,sw}$ = 0.59 (RMSE = 0.06 m; NMSE = 0.07) and $\gamma_{s,ig}$ = 0.61 (RMSE = 0.18 m; NMSE = 0.36). Note that all statistics are significant at the 95% confidence interval or better.

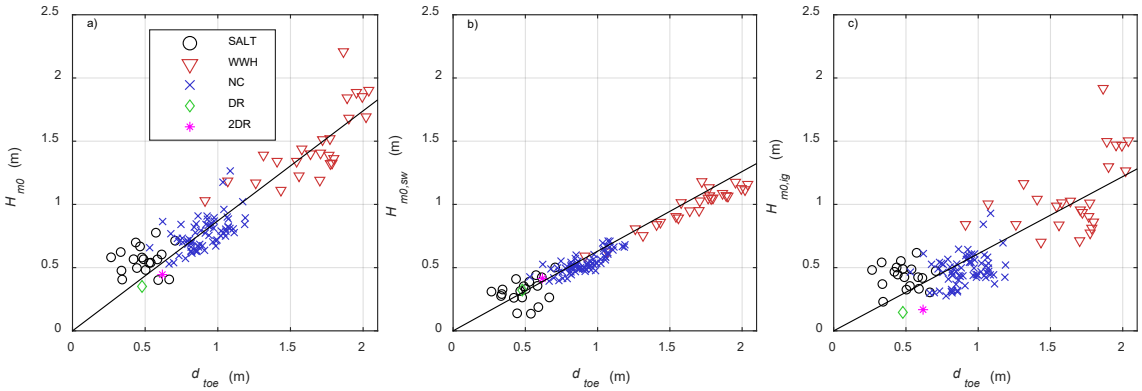

Figure 6: a) Total, **(b)** short-wave, and **(c)** infragravity spectral significant wave height as a function of the water depth above the berm toe. The solid black lines in each plot present the best fit wave height to water depth ratios (γ_s) for each panel (γ_s = 0.87, $\gamma_{s,sw}$ = 0.59 and $\gamma_{s,ig}$ = 0.60).

A relationship between significant swash height S and $H_{m0}\tan\beta_{swash}$ is observed within all frequency bands in Fig. 7. Similar variation of S, S_{sw} and S_{ig} with offshore wave height H_o has been presented previously on a dissipative sand beach by Senechal et al. (2011), however here the wave height at the berm toe is used and a slope term consistent with previous authors (Hunt, 1959; Battjes, 1974; Holman, 1986) has been included. This causes the data from the lower gradient NC experiment to collapse onto that for SALT and WWH. The relationship between S_{sw} and $H_{m0,sw}\tan\beta_{swash}$ is approximately linear. However, there is evidence that S_{ig} (and hence S) increases more slowly with increasing $H_{m0,ig}$ for $H_{m0,ig}\tan\beta_{swash}$ > 0.3 m at WWH, potentially indicating infragravity swash saturation. Comparable results were presented by Senechal et al. (2011) who suggested that significant infragravity swash height may reach a maximum value for large offshore wave heights (H_o > 4 m).

For the current data, a linear regression analysis leads to the following expressions:

$$S = 0.48 + 5.65H_{m0}\tan\beta_{swash} \quad (r^2 = 0.91, \text{RMSE} = 0.20 \text{ m}; \text{NMSE} = 0.10) \quad (8)$$

$$S_{sw} = 0.23 + 6.79H_{m0,sw}\tan\beta_{swash} \quad (r^2 = 0.92, \text{RMSE} = 0.15 \text{ m}; \text{NMSE} = 0.08) \quad (9)$$

$$S_{ig} = 0.48 + 4.59H_{m0,ig}\tan\beta_{swash} \quad (r^2 = 0.85, \text{RMSE} = 0.17 \text{ m}; \text{NMSE} = 0.17) \quad (10)$$

Equations 8-10 include a non-zero intercept which is a common feature of existing wave runup equations for sand beaches (e.g. Guza and Thornton, 1982; Holman, 1986; Ruggerio et al., 2001). On composite beaches, this non-zero intercept may be physical meaningful because when the mean shoreline position is seaward of the berm and the significant wave height at the berm toe is zero, wave runup can still be initiated on the sandy part of the beach and propagate onto the berm.

No dependence of significant swash height on wave period was found within the current dataset in contrast to many previous studies of wave runup (e.g. Guza and Thornton, 1982; Holman, 1986; Ruggerio et al., 2001). For composite beaches it is suggested that this lack of dependence is because significant swash height is controlled by the wave height at the berm toe as shown in Fig 7. For the composite beaches studied here, wave height at the berm toe is depth-limited and previous studies have suggested that wave height to water depth ratio in the inner surf zone is not strongly dependent on wave period on dissipative slopes (e.g. Thornton & Guza, 1982).

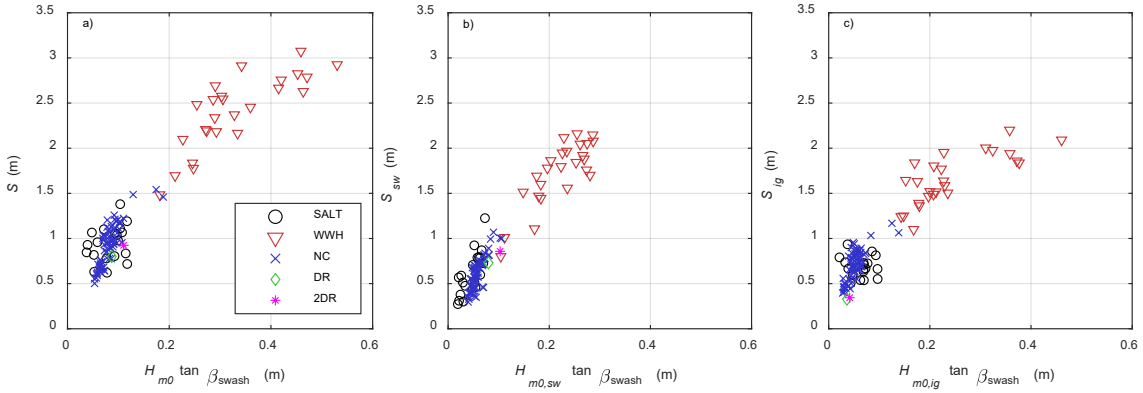

Figure 7: a) Total, **(b)** short-wave, and **(c)** infragravity components of significant swash height as a function of $H_{m0}\tan\beta_{swash}$ where H_{m0} is evaluated within the relevant frequency band (H_{m0}, $H_{m0,sw}$, $H_{m0,ig}$).

4.3 Infragravity wave height at the berm toe

Fig. 7 demonstrates a strong relationship between S and $H_{m0}\tan\beta_{swash}$ in the infragravity and short-wave frequency bands. However, while the spectral significant short-wave height $H_{m0,sw}$ is independent of that in deep water when the surf zone is saturated, infragravity wave height $H_{m0,ig}$ is dependent not only on depth at the berm toe but is also influenced by the offshore wave conditions. Previous authors have shown S_{ig} or $H_{m0,ig}$ to be dependent on offshore wave height H_0 (Guza and Thornton, 1982), wave power (Inch et al. 2017), $\sqrt{H_0 L_0}$ (Stockdon et al., 2006; Fiedler et al., 2015) and $H_0 T_p \sqrt{\tan\beta}$ (Billson et al., 2019). The measured significant infragravity wave height at the berm toe as a function of these parameters are presented for the current data in Fig. 8. All panels in Fig. 8 display scatter, but a dependency of significant infragravity wave height at the berm toe, $H_{m0,ig}$ on H_0 is evident in Fig. 8a. Inch et al. (2017) found good correlation between $H_{m0,ig}$ and both wave height and wave power and provided best-fit linear regressions:

$$H_{m0,ig} = 0.18H_0 + 0.08 \quad (11)$$

$$H_{m0,ig} = 0.004H_0^2 T_p + 0.20 \quad (12)$$

These parameterisations have some predictive ability for the current dataset (Eq. 11: r^2 = 0.40, RMSE = 0.20 m, NMSE = 0.43; Eq. 12: r^2 = 0.65, RMSE = 0.17 m, NMSE = 0.44), but they do not improve on the linear relationship with depth above the berm toe observed in Fig. 6c and discussed in section 4.2 ($\gamma_{s,ig}$ = 0.61). Note that equivalent plots of S_{ig} as a function of these parameters provide a very similar result due to the relationship between $H_{m0,ig}$ and S_{ig} observed in Fig. 7c.

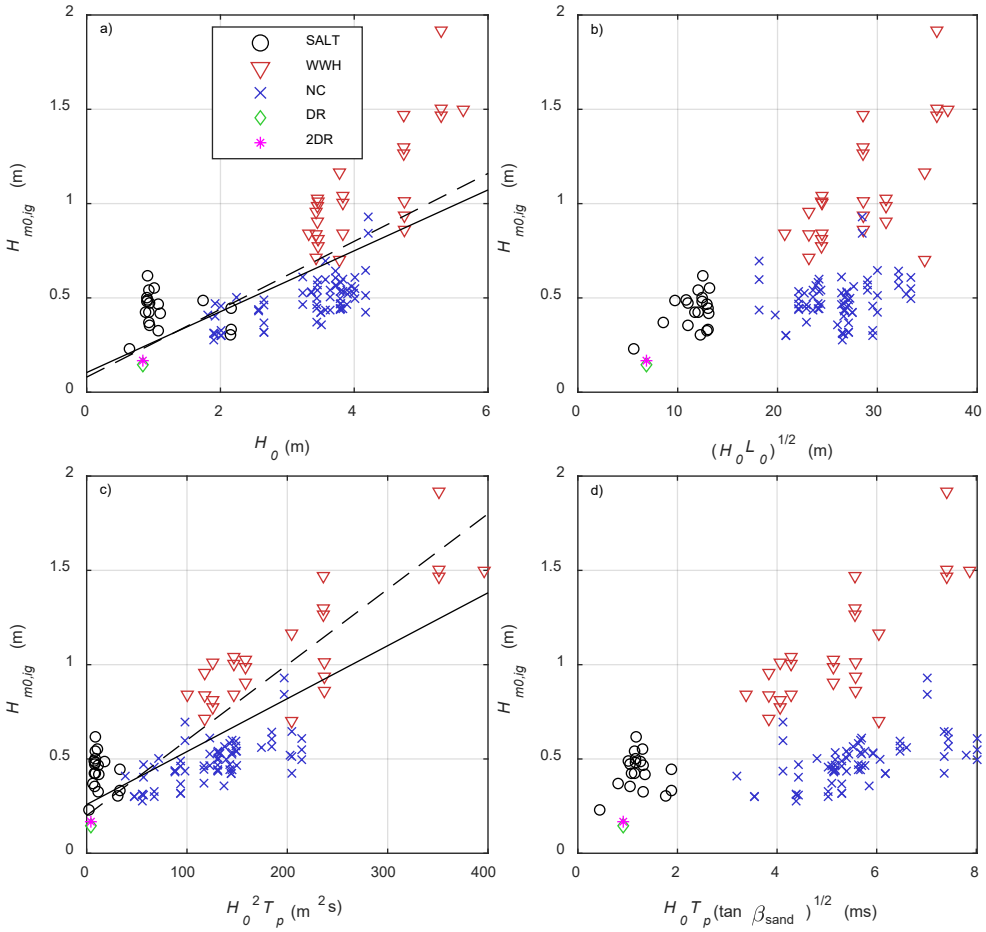

Figure 8: Spectral significant infragravity wave height at the berm toe as a function of previously reported predictors: **(a)** significant offshore wave height (Guza and Thornton, 1982), **(b)** $\sqrt{H_0 L_0}$ (Stockdon et al., 2006), **(c)** $H_0^2 T_p$ (Inch et al. 2017), and **(d)** $H_0 T_p \sqrt{tan\beta}$ (Billson et al., 2019). The dashed lines in panels a and c show the fits obtained by Inch et al. (2017) and the black lines show linear regressions for the current dataset.

Previous authors have suggested that while transfer of energy to infragravity frequencies is greater on low gradient beaches (de Bakker et al., 2015), the rate of infragravity energy dissipation typically increases with reducing depth (Inch et al., 2017). As such, $H_{m0,ig}$ at the shoreline is expected to reduce with increasing surf zone width for a constant value of H_o. Due to the two-slope nature composite beaches with a low gradient foreshore and steep berm, the surf zone width will reduce not only with smaller H_o, but also with increasing water depth over the berm toe for a constant deepwater wave condition. Fig. 9a presents the significant infragravity wave height at the berm as a function of a geometric proxy for composite beach surf zone width, l_{sz}:

$$l_{sz} = \frac{5/3H_o - d_{toe}}{tan\beta_{sand}} + \frac{d_{toe}}{tan\beta_{berm}} \quad (13)$$

where $5/3H_0$ is used to estimate the breaker depth in a saturated surf zone based on Thornton and Guza (1982). It is acknowledged that this approach is simplistic as it does not account for wave shoaling, however it appears to provide reasonable estimates of surf zone width at the three field sites (based on additional Lidar measurements at SALT and visual estimates at WWH and NC) and further refinement to approximate the shoaling process did not improve the results. The line of best fit to the data presented in Fig. 9a is:

$$H_{m0,ig} = 0.0021 l_{sz} + 0.10 \quad (r^2 = 0.74, \text{RMSE} = 0.16 \text{ m}, \text{NMSE} = 0.26) \quad (14)$$

Note that estimating d_{toe} using the SWL elevation ($d_{toe,SWL}$ = SWL-z_{toe}) from measurements obtained seaward of the surf zone rather than MWL_{toe} (hence ignoring wave setup) causes only a small increase in l_{sz} (<5%).

The improved performance of Eq. 14 compared to Eq. 11 or 12 suggests that it is worthy of further investigation over a wider range of conditions because it retains a dependence on offshore wave height (e.g. Fig. 7a: Guza and Thornton, 1982) and explicitly includes beach gradient and surf zone width which are known to influence infragravity wave dissipation. Inch et al. (2017) found that infragravity wave height is better predicted if wave period is accounted for. This was not observed for the data presented here, but should be considered in further investigations with a wider range of sites and wave conditions. A direct relationship between significant infragravity swash height and l_{sz} is also observed in Fig. 9b:

$$S_{ig} = 0.0030 l_{sz} + 0.20 \qquad (r^2 = 0.70, \text{RMSE} = 0.24 \text{ m}, \text{NMSE} = 0.34) \qquad (15)$$

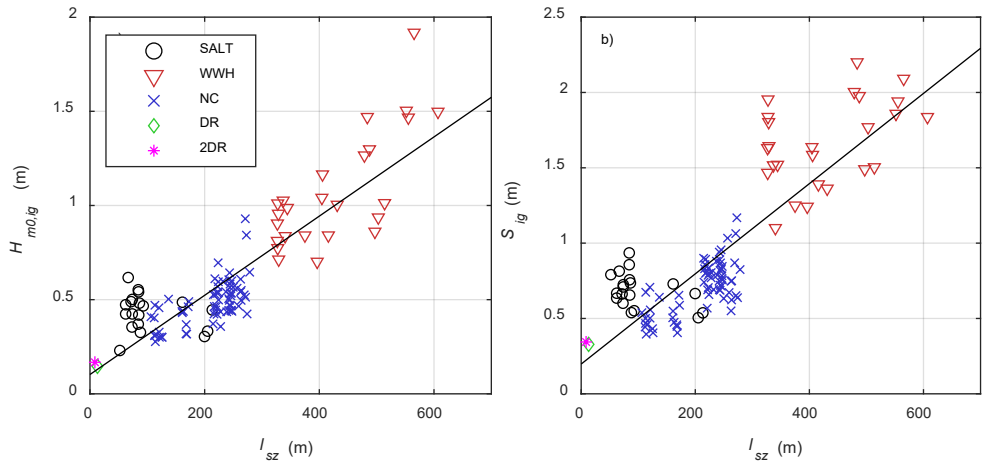

Figure 9: a) Spectral significant infragravity wave height at the berm toe and **(b)** significant infragravity swash height as a function of l_{sz}. The black lines show linear fits to the data.

4. Estimating wave runup on composite beaches

For coastal engineers, the runup parameter of most importance is $R_{2\%}$, the elevation relative to the SWL exceeded by 2% of swash events. This parameter enables an assessment of overtopping risk and is key for assessing the design crest elevation of dynamic cobble berm revetment structures, however to date, no runup equation exists for composite beaches. The following section uses the results presented in Section 4 to develop three new methodologies of varying complexity to predict wave runup on composite beaches and dynamic cobble berm revetments.

For the sites investigated here, there is a strong linear relationship between $R_{2\%}$ and $d_{toe}\tan\beta_{berm}$ when the swash zone occurs entirely on the berm as would be expected during design storm conditions at high tide (Fig. 10a).

$$R_{2\%} = 4.14 d_{toe} \tan\beta_{berm} + 0.66 \qquad (16)$$

It is acknowledged that estimating water depth at the berm toe is not trivial due to wave setup and this is addressed below, however for the data presented here, comparable predictive ability can be achieved using the depth of the berm toe below SWL, $d_{toe,SWL}$ (Fig. 10b) which can be easily estimated.

$$R_{2\%} = 4.59 d_{toe,SWL} \tan\beta_{berm} + 0.75 \quad (17)$$

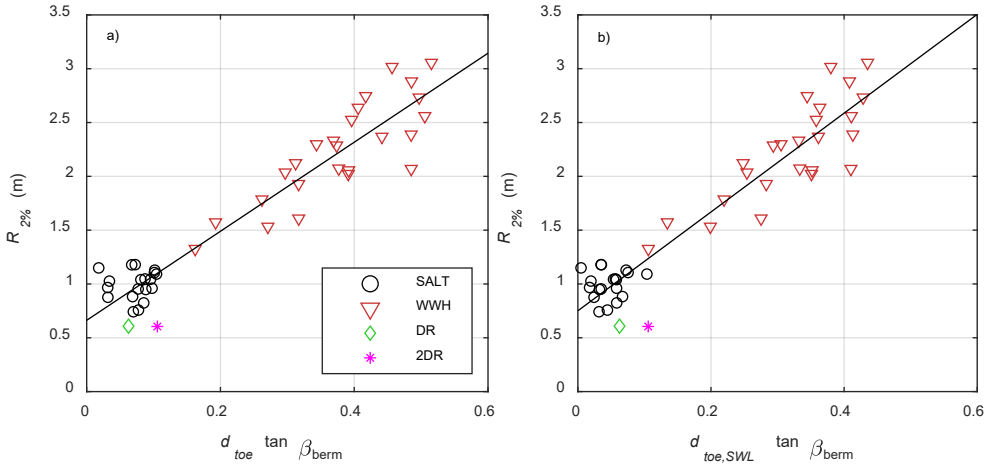

Figure 10: $R_{2\%}$ as a function of **(a)** $d_{toe}tan\beta_{berm}$, and **(b)** $d_{toe,SWL}tan\beta_{berm}$. Note that the NC field data are excluded because no measurement of SWL from seaward of the surf zone was available to enable an estimate of $R_{2\%}$.

While Eq. 16 and 17 provide good predictions for the current dataset (Eq. 16: r^2 = 0.90, RMSE = 0.23 m, NMSE = 0.10; Eq. 17: r^2 = 0.89, RMSE = 0.25 m, NMSE = 0.11), their validity over a wider variety of beach geometry and offshore wave conditions may be more limited. Consequently, a more general approach is outlined below.

As noted in section 3.4, total runup R is composed of a setup $\bar{\eta}$ and swash component S (Eq. 4) and Stockdon et al. (2006) related the statistical runup parameter $R_{2\%}$ to these parameters using field data:

$$R_{2\%} = 1.1\left[\bar{\eta} + \frac{S}{2}\right] \quad (18)$$

Fig. 11 demonstrates that the current data has the same gradient as Eq. 17, but with a non-zero intercept (c = 0.19 m). A non-zero intercept was also found by Stockdon et al. (2006; c = 0.10 m) but they removed it to make Eq. 18 physically consistent. If Eq. 18 is applied to the current dataset, the error statistics (RMSE = 0.28 m, NMSE = 0.16) are only slightly poorer than for the optimum regression line (RMSE = 0.18 m, NMSE = 0.06) and as such it will be used in the following analysis.

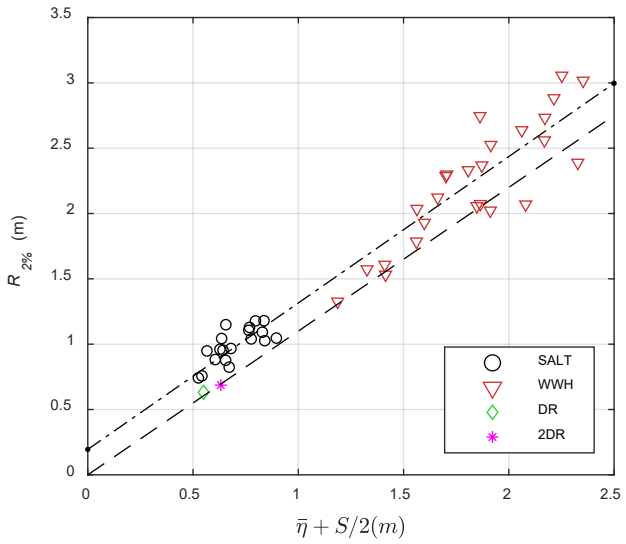

Figure 11: $R_{2\%}$ as a function of the sum of setup and $S/2$. The dashed line represents Eq. 18 (Stockdon et al., 2006) while the dash-dot line is the best fit to the current data with a non-zero intercept (c = 0.19 m).

The wave setup component of runup was shown by Guza and Thornton (1981) to be related to offshore wave height, H_0 and their parameterisation provides a good fit to the current data (r^2 = 0.87, RMSE = 0.10 m, NMSE = 0.19):

$$\bar{\eta} = 0.17H_0 \tag{19}$$

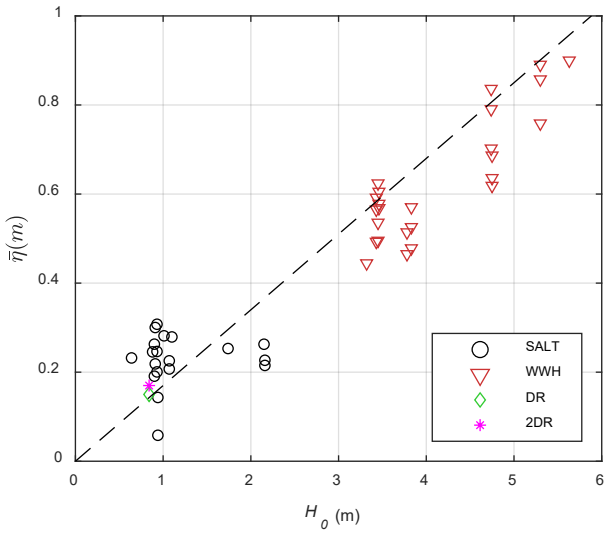

Figure 12: Setup as a function of offshore wave height, where the dashed line represents Eq.18 (Guza and Thornton, 1981).

Combining Eq. 18 and 19 with the previously defined relationship for S as a function of the significant wave height at the berm toe, H_{m0} and $\tan\beta_{swash}$ (Eq. 8), where here we assume that the swash zone is entirely on the berm and so $\tan\beta_{swash} \approx \tan\beta_{berm}$:

$$S = 0.48 + 5.65H_{m0}\tan\beta_{berm} \tag{20}$$

we can obtain an expression to estimate $R_{2\%}$:

$$R_{2\%} = 0.19H_0 + 3.11H_{m0}\tan\beta_{berm} + 0.26 \tag{21}$$

In common with many predictors of wave runup on coastal defence structures (e.g. EurOtop, 2018), a value for the significant wave height at the berm toe H_{m0} is required. It is proposed here that because the sand slope on composite beaches is typically highly dissipative, surf zone waves can reasonably be assumed to be depth-limited so that H_{m0} at the berm toe can be estimated using an appropriate value of wave height to water depth ratio, γ_s. For the current study, the mean measured value of γ_s = 0.87 (see Section 4.2) and this allows H_{m0} to be estimated based on the water depth at the berm toe, d_{toe}. However, it is also noted that the superelevation of the mean water level at the berm toe $\bar{\eta}_{toe}$ is not equal to the setup at the shoreline $\bar{\eta}$ and is required to obtain a suitable value of d_{toe}. For the present data $\bar{\eta}_{toe}$ is best estimated as:

$$\bar{\eta}_{toe} = 3.33 \times 10^{-4} l_{sz} + 0.12 \tag{22}$$

where l_{sz} is obtained using Eq. 13, but using $d_{toe,SWL}$ to approximate d_{toe}. This approach enables d_{toe} to be estimated with an RMSE of just 0.04 m (NMSE = 0.32) where $d_{toe} = d_{toe,SWL} + \bar{\eta}_{toe}$. A flow chart which outlines the suggested methodology to estimate $R_{2\%}$ using Eq. 21 is provided in Figure A1.

A further, more complex approach for estimating $R_{2\%}$ which more explicitly accounts for the short-wave and infragravity components of significant swash height and may be more widely applicable can be defined by decomposing S as shown in Eq. 6 and thus:

$$R_{2\%} = 1.1\left[\bar{\eta} + \frac{\sqrt{S_{sw}^2 + S_{ig}^2}}{2}\right] \quad (23)$$

To apply Eq. 23, $\bar{\eta}$ and S_{sw} can be estimated using Eq. 19 and 8 respectively using $\gamma_{s,sw}$ = 0.59 to obtain $H_{m0,sw}$. At present, the most general approach to estimate S_{ig} is not clear but a range of options exist. For the current dataset, Eq. 10 enables S_{ig} to be predicted with good skill as a function of $H_{m0,ig}$, however as discussed below, there are uncertainties in the estimation of infragravity wave height at the berm toe. As such, Eq. 15 which directly relates S_{ig} to I_{sz} is used to test Eq. 23 (see Figure A2 for a suggested step-by-step approach to apply Eq. 23).

A range of different runup predictors were tested against the measured data (SALT, WWH and DR) and the results are presented in Table 2. As shown by Poate et al (2016), their gravel beach predictor (Eq. 1) greatly overestimated wave runup on a composite beach if the berm slope was used because wave energy dissipation in the surf zone is much lower on a pure gravel beach than on the dissipative sand slope of a composite beach. Much better performance was achieved by setting the slope term in Eq. 1 equal to the sand gradient β_{sand} and the equation is simple to apply, requiring only deepwater data. Nonetheless Eq. 1 underperformed all other methods because it does not account for wave transformation across the dissipative sand slope. The general runup equation presented in EurOtop (2018), Eq. 2 was found to perform poorly for all appropriate values of the roughness factor γ_f, with the best results obtained using γ_f = 0.62 which is at the bottom of the range suggested for dynamic cobble berm revetments by Zaalberg (2019). Despite not being designed for composite beaches, Eq. 3 (EurOtop, 2007) performed well if the empirical constant C_e was reduced from 0.3 to 0.2. It is noted that Eq. 3 does not require a value for the berm gradient which could be advantageous for practising engineers where the slope of an evolving composite beach ridge or dynamic cobble berm revetment may not be known. Caution is suggested however, because the range of berm gradients within the SALT and WWH datasets which were used primarily to test the equations is small ($\tan\beta_{berm}$ = 0.15 to 0.25). Unfortunately, no values of $R_{2\%}$ are available for NC where the berm slope is lower ($\tan\beta_{berm}$ = 0.08 to 0.13) than at the other field sites, however we can obtain further insight into the applicability of Eq. 3 (with C_e= 0.2) for composite beaches with lower gradient berms by analysing the NC dataset. If Eq. 18 is rearranged to make S the subject, we obtain:

$$S = 2\left(\frac{R_{2\%}}{1.1} - 0.17H_0\right) \quad (24)$$

If Eq. 24 is then applied to estimate S at NC using values of $R_{2\%}$ calculated using Eq. 3 (with C_e = 0.2), it has no predictive ability (r^2 = 0.11, RMSE = 1.83 m, NMSE = 72.8). Consequently Eq. 3 cannot be recommended for use on composite beaches based on the current dataset.

The runup equations developed in this paper (eqs. 17, 21 and 23) were all found to have smaller RMS errors than those observed for runup models on sand beaches (e.g. Stockdon et al., 2006; Power et al., 2019) and NMSE values smaller than 0.08. Additionally, the new methods performed better than the previously reported approaches (without modification of the coefficients), though this is partly because they were developed and tested against the same dataset. As expected, Eq. 17 which simply relates $R_{2\%}$ to $d_{toe,SWL}\tan\beta_{berm}$ performed the best because it was fitted directly to the current dataset (excluding NC), however it is unclear whether this will be valid outside of the range of the data presented here. Equations 21 and 23 break down the wave runup into separate setup

and swash components with the aim of making the approach more robust and generally applicable. Both predictors tend to underestimate $R_{2\%}$ because the value of $\gamma_s = 0.87$ and equations 8, 9 and 15 were developed using the entire dataset including the NC data, but no valid measurements of $R_{2\%}$ are available for NC for equation testing. The NC dataset has a tendency for slightly lower values of S_{ig} (Fig. 9b) and γ_s ($\gamma_{s,NC} = 0.85$) which leads to underestimates of H_{m0} used in Eq. 21 and 23 and S_{ig} which is used in Eq. 23.

Due to the uncertainties associated with the prediction of $H_{m0,ig}$, and the contribution of infragravity wave components to both significant wave height and significant swash height, it is presently unclear whether Eq. 21 or 23 is the most general approach for predicting wave runup on composite beaches. Part of this uncertainty arises due to the application of a cutoff frequency to separate, and hence decouple, wave motions at short-wave and infragravity frequencies. Besides inevitably leading to some short-wave energy being assigned to the infragravity band or vice-versa, this separation is fundamentally questionable close to the shoreline, especially during energetic conditions. Additionally, the behaviour of infragravity waves in the nearshore is complex, and parametric models for predicting bulk parameters are far less accurate than in the short-wave frequency band. Infragravity wave heights at the shoreline are strongly influenced by processes such as the transformation of short-waves groups in both shoaling and surf zone regions (Thomson et al., 2006; de Bakker et al., 2015; Mendes et al., 2018) and frequency-dependent reflection observed at low frequencies in the nearshore (Elgar et al., 1994; Sheremet et al., 2002; Bertin et al., 2020). Through their influence on $H_{m0,ig}$, such processes will directly affect the predictive skill of Eq. 21 and 23. From an engineering point of view, Eq. 15 which can be used to directly estimate S_{ig} as a function of surf zone width l_{sz} is potentially valuable when using Eq. 23 since the prediction becomes independent from our limited capacity to predict the wave energy at infragravity frequencies. However, until further work is completed to make progress on these issues, the authors recommend using Eq. 21 to predict wave runup on composite beaches and dynamic cobble berm revetments due to the greater simplicity of this approach.

Table 2: Summary of wave runup equation performance detailing the primary equation used and the secondary equations applied to resolve the input parameters for the primary equation. See Figure A1 and A2 for a step-by-step approach to apply equations 20 and 22.

Source	Primary Eq.	Secondary Eqs.	RMSE (m)	NMSE	Bias (m)
Poate et al. (2016)	1	$\beta = \beta_{berm}$	2.61	12.37	1.24
Poate et al. (2016)	1	$\beta = \beta_{sand}$	0.54	0.53	-0.42
EurOtop (2018)	2	$\gamma_s = 0.87$, $\gamma_f = 0.62$ (Zaalberg, 2019)	0.56	1.59	0.31
EurOtop (2007)	3	22, $\gamma_s = 0.87$, $C_e = 0.3$	0.87	1.47	0.79
EurOtop (2007)	3	22, $\gamma_s = 0.87$, $C_e = 0.2$	0.23	0.10	-0.04
This paper	17		0.23	0.09	-0.04
This paper	21	22, $\gamma_s = 0.87$	0.27	0.14	-0.15
This paper	23	9, 15, 19, 22, $\gamma_{s,sw} = 0.59$	0.33	0.22	-0.19

The three new methods to predict wave runup on composite beaches (Eq. 17, 21 and 23) were developed and tested using the same dataset. This is a common approach for the establishment of wave runup equations and the dataset covered a range of beach geometries, water levels and wave conditions. Nonetheless, it is valuable to investigate the robustness of the fits provided, and the variability of the regression coefficients by re-fitting key equations using a subset of the complete dataset. In the analysis below, the complete dataset was split at random into separate training and validation datasets containing 75% and 25% of the data respectively. This process was repeated to generate 100 different training and validation subsets. For each training dataset, linear regressions

were performed to re-fit runup equations 17 and 21, as well as equations 9 and 15 which are the key parameterisations needed to apply Eq. 23. The performance of these equations was then evaluated using the validation dataset.

It is evident from the summary of results presented in Table 3 that the mean values of gradient and intercept obtained from this process are almost identical to those in the original equations and the relative standard deviation is small (< 5%) except for the intercept of Eq. 15. For the intercept of Eq. 15, the standard deviation is small in absolute terms (0.03 m) and the apparently large relative standard deviation is due to the small value of the mean. RMSE values are within 10% of those obtained for the original equations. The RMSE values for both the training and validation datasets are comparable and in line with the values for the entire dataset, indicating that the fits presented above are reasonably robust and not highly sensitive to the exact data used for the fitting process.

Table 3: Summary of re-fitting analysis completed for key equations. Mean and relative standard deviation values [in square brackets] are shown for the gradient and intercept of each equation. The mean and relative standard deviation of the RMSE for both the training ($RMSE_{train}$) and validation ($RMSE_{val}$) datasets are also given.

Eq.	Gradient, m [RSD]	Intercept, c [RSD] (m)	$RMSE_{train}$ [RSD] (m)	$RMSE_{val}$ [RSD] (m)
9	6.80 [2.1%]	0.23 [4.4%]	0.15 [6.7%]	0.13 [7.7%]
15	0.003 [4.2%]	0.19 [16%]	0.25 [3.8%]	0.20 [7.0%]
17	4.60 [2.8%]	0.74 [4.1%]	0.25 [8.0%]	0.24 [20.8%]
21	3.11 [2.6%]	0.26 [3.9%]	0.31 [4.9%]	0.31 [15.0%]

A further evaluation of the potential performance of the new methods for data from outside of the parameter space used to develop the equations was also undertaken. The data corresponding to the highest energy conditions (WWH, 2nd November) were removed as a validation dataset, with the remainder used for training. The results of this process are shown in Table 4. It is evident that the re-fitted equations are able to predict wave runup for the whole $R_{2\%}$ dataset (SALT, WWH, 1DR and 2DR) with a comparable precision to the original forms of equations 17, 21 and 23. Furthermore, when tested against the high-energy validation data subset, only a slightly increased RMSE and marginally greater negative bias is observed. NMSE values are mostly smaller due to the reduced range of values covered by the validation dataset. While it is recommended that the methods developed in this study should be thoroughly tested against new datasets as they become available, this result gives some confidence that all three are reasonably robust and capture the main processes causing wave runup on composite beaches.

Table 4: Summary of re-fitted wave runup equation performance. Statistical parameters are given for the entire $R_{2\%}$ dataset and the high-energy validation subset (WWH, 2nd November) [square brackets].

Re-fitted Eq.	RMSE (m)	NMSE	Bias (m)
17	0.24 [0.30]	0.11 [0.12]	-0.09 [-0.20]
21	0.24 [0.28]	0.11 [0.04]	-0.12 [-0.14]
23	0.31 [0.38]	0.18 [0.07]	-0.17 [-0.29]

5. Conclusions

This paper describes new measurements of swash using 2D scanning Lidar on composite beaches and dynamic revetments during a series of field and large-scale laboratory experiments.

It was demonstrated that the significant swash height *S* increases substantially as the swash zone moves from the dissipative sand beach to the reflective gravel berm during a rising tide. When the swash zone is on the sand beach, the total significant swash height is dominated by swash motions

at infragravity frequencies (S_{ig}), however as the berm toe becomes submerged, the significant short-wave swash height S_{sw} increases rapidly, leading to the observed increase in total significant swash height.

The wave height at the toe of composite beach berms and dynamic revetments is decoupled from the offshore wave conditions and primarily controlled by the water depth at the berm toe during high tides when inundation risk is greatest due to the dissipative nature of the fronting sand beach. As a result, significant swash height was found to be highly correlated to water depth, particularly at short-wave frequencies. Infragravity wave height at the berm toe, and hence significant infragravity swash was also found to vary with water depth. There is evidence that this is due to the changing surf zone width with water level on the two-slope composite beach geometry.

Based on the new insight gained from the experimental results, three new methods with differing complexity were developed to predict wave runup on composite beaches and dynamic revetments incorporating wave setup, short-wave and infragravity swash components. These new composite beach-specific methods were found to provide good predictions of extreme wave runup and will enable more robust design of dynamic cobble berm revetements and assessment of coastal hazards at composite beaches. It was noted however that the proposed methods are partly restricted by uncertainties related to infragravity swash motions and further research in this area will be valuable.

Acknowledgements

The authors would like to acknowledge the support of everyone who assisted with the field and laboratory experiments reported here, in particular Jack Puleo, Brittany Bruder and Hannah Power (SALT), David Cottrell and Heather Weiner (NC), Gerd Masselink, Tim Poate and Kris Inch (WWH), Matthias Kudella, Isabel Kelly, Emily Gulson and Tom Beuzen (DR1 and 2). The SALT experiment was funded by the Engineering and Physical Sciences Research Council (EPSRC) grant EP/N019237/1, Waves in Shallow Water, awarded to Chris Blenkinsopp. WWH was funded by Engineering and Physical Sciences Research Council (EPSRC; EP/H040056/1). DynaRev1 received funding from the European Union's Horizon 2020 research and innovation programme under grant agreement No 654110, HYDRALAB+. DynaRev2 was funded through a Research England Global Challenges Research Fund. Chris Blenkinsopp was supported by a Royal Academy of Engineering Leverhulme Trust Research Fellowship. Ollie Foss and Paul Bayle were supported by a PhD scholarship through the EPSRC CDT in Water Informatics: Science and Engineering (WISE). Kévin Martins acknowledges financial support from the University of Bordeaux, through an International Postdoctoral Grant (Idex, nb. 1024R-5030). Hironori Matsumoto was supported by U.S. Army Corp of Engineers (W912HZ192) and the California Department of Parks and Recreation, Natural Resources Division Oceanography Program (C19E0026).

Appendices

Table A1: List of symbols.

Symbol	Definition
d_{toe}	Water depth above berm toe (m)
$d_{toe,SWL}$	Vertical elevation difference between berm toe and SWL (m)
D_n	Sediment diameter exceeded by *n*% of particles
H_o	Significant wave height measured offshore (m)
H_{m0}	Spectral significant wave height at berm or structure toe (m)
$H_{m0,sw}$	Short wave spectral significant wave height at berm or structure toe (m)
$H_{m0,ig}$	Infragravity spectral significant wave height at berm or structure toe (m)

K	
L_o	Deep water wavelength (m)
l_{sz}	Composite beach surf zone width (m)
MWL_{toe}	Mean water surface elevation at the berm toe within 10-minute time windows (m)
$R_{2\%}$	Runup elevation exceeded by 2% of incident waves (m)
S	Total significant swash height (m)
S_{sw}	Significant short wave swash height (m)
S_{ig}	Significant infragravity swash height (m)
s_{om}	Wave steepness calculated using T_z
SWL	Mean water surface elevation seaward of the surf zone within 10-minute time windows (m)
T_z	Mean zero-crossing wave period (s)
T_p	Spectral peak wave period (s)
$T_{m-1,0}$	Mean spectral wave period (s)
X_s	Horizontal shoreline position (m)
Z_s	Vertical shoreline position (m)
z	Vertical elevation above datum (m)
z_{toe}	Elevation of berm toe above datum (m)
z_{WL}	Water depth above flume bed at DR and 2DR (m)
β_{sand}	Angle between the mean sand beach slope and horizontal
β_{berm}	Angle between the mean gravel berm slope and horizontal
β_{struct}	Angle between coastal structure slope and horizontal
β_{gravel}	Angle between mean pure gravel beach slope and horizontal
β_{swash}	Angle between the mean swash slope and horizontal within a 10-minute time window
$\bar{\eta}$	Wave setup at the shoreline (m)
$\bar{\eta}_{toe}$	Superelevation of the mean water level at the berm toe due to wave setup (m)
γ_f	Reduction factor to account for the slope roughness in Eq. 2
γ_s	Wave height to water depth ratio at the berm toe
$\gamma_{s,sw}$	Short wave height to water depth ratio at the berm toe
$\gamma_{s,ig}$	Infragravity wave height to water depth ratio at the berm toe
ζ	Linearly detrended shoreline elevation

694

695

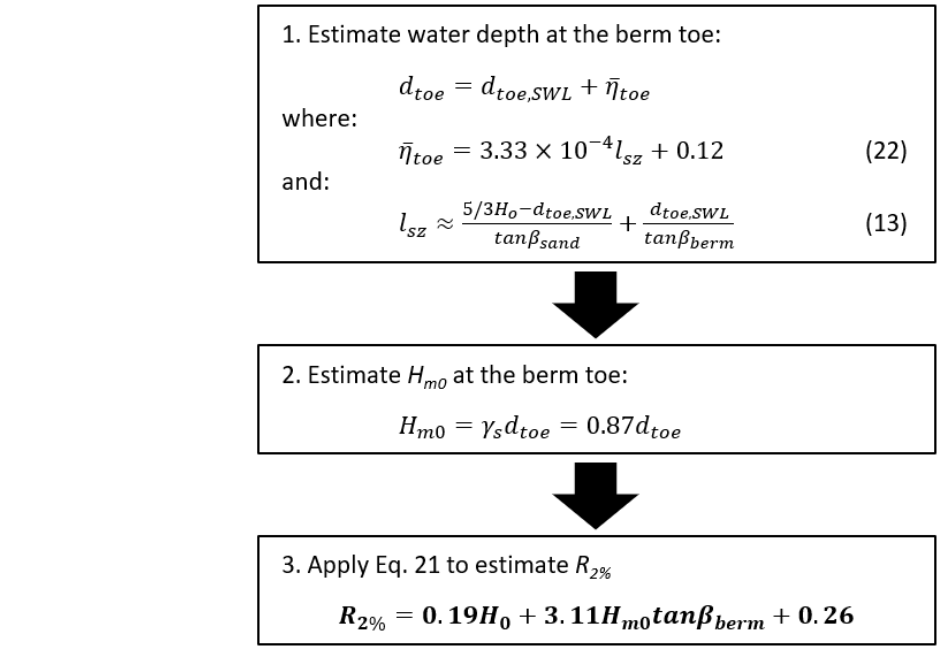

Figure A1: Suggested step-by-step procedure for application of Eq. 21.

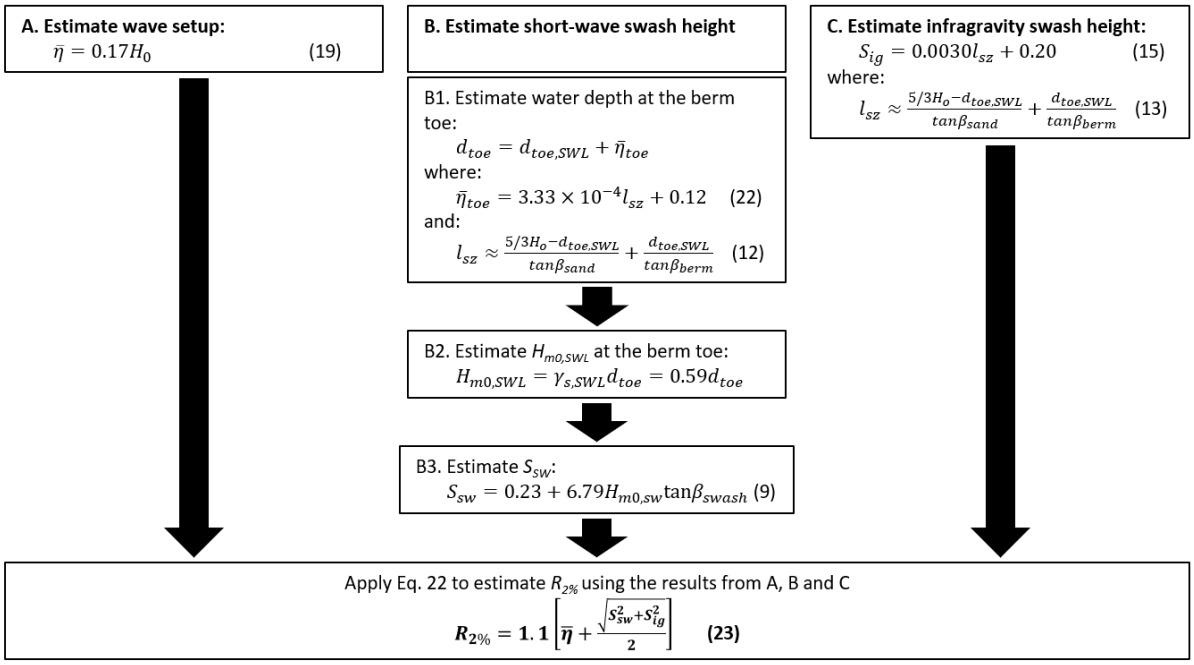

Figure A2: Suggested step-by-step procedure for application of Eq. 23.

References

Allan, J.C., Geitgey, R., Hart, R. 2005. Dynamic revetments for coastal erosion stabilization: a feasible analysis for application on the Oregon coast. Oregon Department of Geology and Mineral Industries, Special issue 37.

Allan, J.C., Harris, E., Stephensen, S., Politano, V., Laboratory, H., Folger, C., Nelson, W. 2012. Hatfield Marine Science Center Dynamic Revetment Project. Technical Report Hatfield Marine Science Center, Oregon State University.

Almar, R., Blenkinsopp, C.E., Almeida, L.P, Cienfuegos, R., Catalan, P. 2017. Wave runup video motion detection using the Radon Transform. Coast. Eng., 130, 46-51.

Almeida, L.P., Masselink, G., Russell, P.E., Davidson, M.A. 2015. Observations of gravel beach dynamics during high energy wave conditions using a laser scanner. Geomorphology 228, 15-27.

Almeida, L.P., Masselink, G., McCall, R., Russell, P. 2017. Storm overwash of a gravel barrier: Field measurements and XBeach-G modelling. Coast. Eng., 120, 22-35.

Battjes, J.A., 1974. Computation of set-up, longshore currents, run-up and overtopping due to wind-generated waves. Report 74-2, Committee on Hydraulics, Department of Civil Engineering. Delft University of Technology, Delft, The Netherlands.

Bayle, P.M., Blenkinsopp, C.E., Conley, D., Masselink, G., Beuzen, T., Almar, R. 2020. Performance of a dynamic cobble berm revetment for coastal protection, under increasing water level. Coast. Eng. 159, 103712.

Bayle, P.M., Kaminsky, G.M., Blenkinsopp, C.E., Weiner, H.M., Cottrell, D. 2021. Behaviour and performance of a dynamic cobble berm revetment during a spring tidal cycle in North Cove, Washington State, USA. Coast. Eng. 167: 103898. https://doi.org/10.1016/j.coastaleng.2021.103898

Bertin, X., Martins, K., de Bakker, A., Chataigner, T., Guérin, T., Coulombier, T., and de Viron, O., 2020. Energy Transfers and Reflection of Infragravity Waves at a Dissipative Beach Under Storm Waves. J. Geophys. Res. Oceans 125(5), e2019JC015714. doi: 10.1029/2019JC015714.

Billson, O., Russell, P.E. Davidson, M. 2019. Storm Waves at the Shoreline: When and Where Are Infragravity Waves Important? J. Mar. Sci. Eng. 7(5), 139; https://doi.org/10.3390/jmse7050139.

Blenkinsopp, C.E., Mole, M.A., Turner, I.L., Peirson, W.A. 2010. Measurements of the time-varying free-surface profile across the swash zone obtained using an industrial LIDAR. Coast. Eng. 57(11-12), 1059-1065.

Blenkinsopp, C.E., Matias, A., Howe, D., Castelle, B., Marieu, V., Turner, I. L. 2016. Wave runup and overwash on a prototype-scale sand barrier. Coast. Eng., 113, pp. 88-103.

Blenkinsopp, C.E., Bayle, P.M, Conley, D.C., Masselink, G., Gulson, E., Kelly, I., Almar, R., Turner, I.L., Baldock, T.E., Beuzen, T., McCall, R.T., Rijper, H., Reniers, A., Troch, P., Gallach-Sanchez, D., Hunter, A.J., Bryan, O., Hennessey, G., Ganderton, P., Tissier, M., Kudella, M., Schimmels, S. 2021 High-resolution, large-scale laboratory measurements of a sandy beach and dynamic cobble berm revetment. Scientific Data 8(1), 10.1038/s41597-021-00805-1.

Bonneton, P., Lannes, D., Martins, K., Michallet, H. (2018). A non-linear weakly dispersive method for recovering the elevation of irrotational surface waves from pressure measurements. Coast. Eng., 138, 1–8. https://doi.org/10.1016/j.coastaleng.2018.04.005

Brodie, K. L., Slocum, R. K., McNinch, J. E. 2012. New insights into the physical drivers of wave runup from a continuously operating terrestrial laser scanner. Oceans 2012, 1 – 8. doi: 10.1109/OCEANS.2012.6404955.

Brodie, K.L. Raubenheimer, B. Elgar, S. Slocum, R.K. McNinch, J.E. 2015. Lidar and pressure measurements of inner-surfzone waves and setup. J. Atmos. Ocean. Technol. 32, 1945–1959.

745 Carter, R.W.G., Orford, J.D. 1993 The morphodynamics of coarse clastic beaches and barriers: a short
746 and long term perspective. *Journal of Coastal Research* 15, 158-179.

747 De Bakker, A. T. M., Herbers, T. H. C., Smit, P. B., Tissier, M. F. S., & Ruessink, B. G. 2015. Nonlinear
748 infragravity-wave interactions on a gently sloping laboratory beach. J. Phys. Oceanogr. 45(2), 589–
749 605. https://doi.org/10.1175/JPO-D-14-0186.1

750 Elgar, S., Herbers, T.H.C., Guza, R.T., 1994. Reflection of Ocean Surface Gravity Waves from a Natural
751 Beach. J. Phys. Oceanogr. 24, https://doi.org/10.1175/1520-
752 0485(1994)024<1503:ROOSGW>2.0.CO;2

753 EurOtop. 2007. Wave overtopping of sea defences and related structures - Assessment Manual. UK:
754 N.W.H. Allsop, T. Pullen, T. Bruce. NL: J.W. van der Meer. DE: H. Schuttrumpf, A. Kortenhaus.
755 www.overtopping-manual.com.

756 EurOtop, 2018. Manual on wave overtopping of sea defences and related structures. An overtopping
757 manual largely based on European research, but for worldwide application. Van der Meer, J.W.,
758 Allsop, N.W.H., Bruce, T., De Rouck, J., Kortenhaus, A., Pullen, T., Schüttrumpf, H., Troch, P. and
759 Zanuttigh, B., www.overtopping-manual.com.

760 Everts, C.H., Eldon, C.D., Moore, J., 2002. Performance of cobble berms in southern California. Shore
761 and Beach 70 (4), 5–14.

762 Fiedler, J., Brodie, K.L., McNinch, J.E. and Guza, R.T. 2015. Observations of runup and energy flux on
763 a low-slope beach with high-energy, long-period ocean swell. Geophys. Res. Letters 42(22), 9933-
764 9941.

765 Guedes, R. M., Bryan, K. R., Coco, G. 2012. Observations of alongshore variability of swash motions
766 on an intermediate beach. Cont. Shelf Res. 48, 61 – 74. doi:10.1016/j.csr.2012.08.022.

767 Guza, R.T., Thornton, E.B., 1981. Wave set-up on a natural beach. J. Geophys. Res. Oceans 86 (C5),
768 4133–4137.

769 Guza, R.T., Thornton, E.B., 1982. Swash oscillations on a natural beach. J. Geophys. Res. Oceans 87,
770 483–491.

771 Hamm, L., Peronnard, C., 1997. Wave parameters in the nearshore: A clarification. Coast. Eng. 32 (2-
772 3), 119–135.

773 Holman, R.A., 1986. Extreme value statistics for wave run-up on a natural beach. Coast. Eng. 9, 527-
774 544.

775 Hofland, B., Diamantidou, van Steeg, P., Meys, P. 2015. Wave runup and wave overtopping
776 measurements using a laser scanner. Coast. Eng. 106, 20-29.

777 Hunt, I.A., 1959. Design of seawalls and breakwaters. J. Waterw. Harb.Div. 85 (WW3), 123–152.

778 Inch, K., Davidson, M., Masselink, G., Russell, P.E. 2017. Observations of nearshore infragravity wave
779 dynamics under high energy swell and wind-wave conditions. Cont. Shelf Res. 138, 19-31.

780 Jennings, R., Schulmeister, J. 2002. A field based classification scheme for gravel beaches. Mar. Geol.,
781 186, 211- 228.

Kaminsky, G., Cottrell, D., Glore, G. 2020. Nature-based dynamic revetment construction at North Cove, Washington, USA. Coastal Engineering Proceedings, (36v), management.38. https://doi.org/10.9753/icce.v36v.management.38

Karunarathna, H., Horrillo-Caraballo, J.M., Ranasinghe, R., Short, A.D., Reeve, D.E. 2012 An analysis of the cross-shore beach morphodynamics of a sandy and a composite gravel beach. Mar. Geol., 299, 33-42. (doi:10.1016/j.margeo.2011.12.011)

Kirk, R. M. 1975. Aspects of Surf and Runup Processes on Mixed Sand and Gravel Beaches. Geografiska Annaler. Series A, Physical Geography, 57(1/2), 117. doi:10.2307/520532

Komar, P.D. 2005. Hawke's Bay, New Zealand: Environmental Change, Shoreline Erosion and Management Issues. Report for the Hawke's Bay Regional Council, 244p.

Komar, P., Allan, J. C. 2010. Design with nature strategies for shore protection - the construction of a cobble berm and artificial dune in an Oregon state park. In Puget Sound Shorelines and the Impacts of Armoring, Proceedings of a State of the Science Workshop, U.S. Geological Survey Scientific Investigations Report 2010-5254, 117-126.

Martins, K., Blenkinsopp, C.E., Power, H. E., Bruder, B., Puleo, J., Bergsma, E.W.J. 2017a. High-resolution monitoring of wave transformation in the surf zone using a LiDAR scanner array. Coast. Eng., 128, 37-43.

Martins, K., Blenkinsopp, C.E., Almar, R., Zang, J. 2017b. The influence of swash-based reflection on surf zone hydrodynamics: a wave-by-wave approach. Coast. Eng., 122, 27-43.

Martins, K., Blenkinsopp, C.E., Deigaard, R., Power, H. E. 2018. Energy dissipation in the inner surf zone: new insights from LiDAR-based roller geometry measurements. J. Geophys. Res: Oceans, https://doi.org/10.1029/2017JC013369.

Mason, T., Coates, T.T. 2001. Sediment transport processes on mixed beaches: A review for shoreline management. J. Coast. Res., 17, 645–657.

Masselink, G. Li, L., 2001. The role of swash infiltration in determining the beachface gradient: a numerical study. Mar. Geol. 176, 139-156.

Matsumoto, H., Young, A. P., Guza, R. T. 2020a. Observations of surface cobbles at two southern California beaches. Mar. Geol., 419, 106049. https://doi.org/10.1016/j.margeo.2019.106049

Oh, J.-E., Jeong, W.-M., Chang, Y.S., Oh, S.-H. On the Separation Period Discriminating Gravity and Infragravity Waves off Gyeongpo Beach, Korea. J. Mar. Sci. Eng. 2020, 8, 167. https://doi.org/10.3390/jmse8030167.

Poate, T.G., McCall, R,T., Masselink, G. 2016. A new parameterisation for runup on gravel beaches. Coast. Eng. 117, 176-190 https://doi.org/10.1016/j.coastaleng.2016.08.003.

Polidoro, A., Pullen, T., Dornbusch, U., 2014. Wave run-up on shingle beaches – a new method. HR Wallingford Technical Report CAS0942-RT001-R05-00: Wallingford, UK, 2014.

Powell, K.A., 1990. Predicting Short Term Profile Response for Shingle Beaches. Hydraulics Research Limited, Wallingford, Oxfordshire. Report SR2 19.

819 Raubenheimer, B., Guza, R.T., Elgar, S. 1996. Wave transformation across the inner surf zone. J.
820 Geophys. Res. Oceans 101(C11), 25589-25597.

821 Ruggiero, P., Komar, P.D., McDougal, W.G., Marra, J.J., Beach, R.A., 2001. Wave runup, extreme
822 water levels and the erosion of properties backing beaches. J. Coast. Res. 17, 407–419.

823 Sallenger, A. H., Holman R. A. 1985. Wave energy saturation on a natural beach of variable slope. J.
824 Geophys. Res., 90(C6), 11,939–11,944.

825 Sénéchal, N., Coco, G., Bryan, K., Holman, R.A. 2011. Wave runup during extreme storm conditions.
826 J. Geophys. Res. 116, C07032, doi:10.1029/2010JC006819.

827 Sheremet, A., Guza, R.T., Elgar, S., Herbers, T.H.C., 2002. Observations of nearshore infragravity
828 waves: Seaward and shoreward propagating components. J. Geophys. Res. 107.
829 doi:10.1029/2001JC000970.C8.

830 Stockdon, H.F., Holman, R.A., Howd, P.A., Sallenger, A.H., 2006. Empirical parameterization of setup,
831 swash and runup. Coast. Eng. 53 (7), 573–588.

832 Thornton, E.B., Guza, R.T. 1982. Energy saturation and phase speeds measured on a natural beach. J.
833 Geophys. Res. Atmos. 87(C12), 9499-9508.

834 Tomasicchio, G.R., D'Alessandro, F., Musci, E. 2010. A multi-layer capping of a coastal area
835 contaminated with materials dangerous to health. Chem Ecol. 26, 155–168.

836 Watt, T., Robinson, D., Moses, C., Dornbusch, U. 2008. Patterns of surface sediment grain size
837 distribution under the influence of varying wave conditions on a mixed sediment beach at Pevensey
838 Bay, southeast England. Zeitschrift fur Geomorphologie, 52 (S3). 63-77.

839 Wentworth, C.K. 1922. A scale of grade and class terms for clastic sediments. The Journal of Geology,
840 30(5), 377-392.

841 Wright, L.D. Short, A.D. 1984 Morphodynamic variability of surf zones and beaches: a synthesis. Mar.
842 Geol., 56, 93-118.

843 Zaalberg, P. 2019. The relation between cobble revetments, sand and overtopping: A numerical
844 approach with OpenFOAM. Unpubl. PhD thesis, Delft University of Technology.